Electronic excitations on metal surfaces and nano-structures

S. R. Barman

Surface Physics Laboratory, UGC–DAE Consortium for Scientific Research, University Campus, Khandwa Road, Indore 452 017, India

Collective electron excitations on a free-electron-like metal surface like Al have been studied by X-ray photoemission spectroscopy. In this review, we discuss photoemission studies on quantization of electron states due to confinement in nano-structures like epitaxial Na films on Al(111). The electronic structure of Ar nano-bubbles embedded in the sub-surface region of Al has been discussed. For Al, an asymmetric line-shape is observed for both monopole surface and bulk plasmon in good agreement with theory. The relative contributions of the intrinsic, extrinsic and the interference processes to the surface plasmon intensity are determined from theoretical plasmon line-shape calculations and angle-dependent photoemission. The characteristics of the multipole plasmon mode are also discussed. Using angle resolved photoemission, Na thin films on Al(111) have been studied for different thicknesses. We find features in the valence band spectra that behave like quantum well resonances in a narrow photon energy range where the overlayer collective excitations are observed. These resonances are observed because of quantum confinement due to a potential step at the Na/Al interface and the dynamical enhancement of the electric field in the overlayer. In case of argon nano-bubbles in Al, we find that the Ar 2p binding energy and the Doniach–Sunjic asymmetry of the core level line shape vary systematically as functions of Ar^+ implantation energy and number of ions bombarded (fluence). These observations are explained by relating the strength of Al conduction electron screening of the core-hole created in the photoemission final state to the size of the Ar nano-bubbles.

PHOTOEMISSION spectroscopy is the most versatile technique to study single particle and collective electron excitations on metal surfaces and nano-structures. Plasmons are collective oscillations of electrons in a solid. Plasmon loss features in the photoemission spectra of metals have been extensively studied from early days of photoemission[1–24]. Bulk plasmons are longitudinal oscillation modes of the electron gas in the solid. The bulk plasmon frequency (w_p) is given by $e = 0$, where e is the bulk dielectric function. The monopole surface plasmon is an oscillating sheet of charge located at the surface, although its energy is dictated by the bulk property ($e = -1$). In the direction perpendicular to the surface (z-direction), the charge distribution of the surface plasmon has a monopolar character and hence it is referred to as the monopole surface plasmon[25,26]. The physics of plasmon excitations in photoemission is interesting because different processes contribute to its intensity. The sudden change in the potential due to creation of a core-hole attracts conduction electrons to screen the core-hole resulting in the intrinsic plasmon excitation[1,2]. On the other hand, extrinsic plasmon excitation results from Coulomb interaction of the conduction electrons with the photoelectron traversing through the solid from the photoemission site to the surface. Besides, an interference process occurs due to quantum interference between the intrinsic and extrinsic plasmons. The interference effect can be visualized as the interaction between the localized photo-hole (intrinsic) and the outgoing photoelectron (extrinsic) in which the virtual plasmon created by one is absorbed by the other[2]. Studies of such collective excitations are important for interpretation of all surface spectroscopies that use electromagnetic fields or charged particles. In angle resolved photoemission (ARPES), surface screening effects can alter the line shape of the direct transition from Ag(111) s band[27,28]. A strong modification of the photoemission line shape has been found in Li near its bulk plasmon frequency[29]. Thus, surface screening effects can influence the spectral line shape in ARPES.

As mentioned earlier, in the z-direction the charge distribution of the monopole surface plasmon has monopolar character[25,26]. On the contrary, there can be higher oscillation modes on the surface whose charge distribution in the z-direction can have a node, i.e. of dipolar or multipolar form. This is the multipole plasmon mode (w_m), which exists on metal surfaces[25,26,30–35]. The multipole surface plasmon cannot be explained by the classical Fresnel theory and the deviation from Fresnel field is given by the d-parameters[25]. $d_\perp(w)$ represents the centroid of the screening density induced by a uniform field oriented normal to the surface. The total surface photoyield is proportional to Im $d_\perp(w)$. Parallel to the surface, both the surface and the multipole plasmons propagate like plane waves with alternate positive and negative regions. Thus, along the surface both the modes are dipolar in nature. The surface plasmon has a negative dispersion at small q, while the multipole plasmon has a positive dispersion[35].

Photoemission technique has been extensively used for studying the electronic properties of nano structures. Angle-

e-mail: barman@udc.ernet.in

resolved photoemission is an ideal technique to examine the dependence of quantum well states on film thickness, substrate and overlayer band structure and quantum well interaction. Many aspects of the electronic structure of thin metal films on different substrates have been investigated in detail[36]. Generally speaking, the confining potential comprises the vacuum barrier on one side, and a reflective barrier such as an absolute or relative gap in the band structure of the substrate on the other. The appearance of quantum well states is usually interpreted in terms of a straightforward ground state picture, i.e. as confinement of electronic states by the bounding potential barriers.

The electronic properties of nano structures can be studied by X-ray photoemission spectroscopy (XPS) through changes in the core level peak position and line-shapes. Implanted Ar ions form nano bubbles in Al due to their repulsive pseudopotential[37]. These bubbles exhibit different interesting phenomena. For example, it is reported that Ar bubbles exist in the solid state even at room temperature and are over-pressurized and have high melting temperature[38–41]. He bubbles are reported to form at high mass densities[42]. Scanning tunnelling microscopy (STM) studies on these bubbles have shown evidence of electron interference between the sub-surface Ar bubbles and the Al surface[42]. Ar bubbles in Al is also an ideal system to study the response of conduction electrons in a nearly free electron metal to a core-hole generated by photoemission in an inert solid bubble of nano-meter size implanted in the metal. An estimate of the bubble size is of importance in different fields like sputter growth of thin films, electromigration failure in conduction lines of integrated circuits, life time of reactor walls, etc[44].

In this review, we deal with specific topics based on our work in electronic structure of solids using photoemission. We first discuss the collective plasmon excitations in Al(111). Next, ARPES studies on quantum well resonances in epitaxial Na films of nanometer thickness are discussed. Finally, we report our recent work on Ar nanobubbles in Al(111).

Collective excitations on Al(111) surface

Plasmon loss features in XPS of free electron-like metals like Al, Mg have been studied by many groups. Early XPS studies on Al, Na and Mg found that the intrinsic plasmon excitation was almost absent in these metals[3]. But, this result contradicted theoretical prediction for the existence of intrinsic plasmon[1,2,20]. However, Fuggle *et al.*[4] found some evidence of intrinsic plasmon in Al layers deposited on Mn. Baird *et al.*[8] found that the surface plasmon intensity is markedly enhanced at low photoelectron emission angle, q. They determined the intensity variation of $1w_p$, $2w_p$ and $1w_s$ and compared them with theoretical calculations based on a jellium model. On the basis of semi-classical calculations, it was shown by Bradshaw *et al.*[7] that in the high photoelectron velocity limit, the intrinsic and the interference contributions are independent of q and that the extrinsic contribution varies as $1/\sin q$. They found a small intrinsic plasmon contribution to the surface plasmon intensity.

Many theoretical studies have been performed to evaluate the contribution of the intrinsic and the extrinsic processes and understand their origin in photoemission[1,2,14–24]. Chang and Langreth have treated the inelastic plasmon losses as a many body effect in the photoemission process and have included the effects of solid surface and the core-hole[2,14]. Sunjic *et al.*[18,19] used an electron–plasmon interaction model for fast electrons and considered the effect of localized core-holes to provide a quantitative description of multiple bulk and surface plasmon processes in metals. Penn[20] calculated the plasmon line-shapes and estimated the intrinsic bulk plasmon contribution to be 26% for Al, which was much lower than 50% intrinsic plasmon contribution suggested by Lundqvist[1]. Inglesfield used the Golden rule formalism of photoemission and considered plasmon dispersion as well as interference effect. Inglesfield studied the suppression of the plasmon intensities at low electron kinetic energies by calculating the plasmon line-shapes as function of kinetic energy and depth of the site of photoemission[21,22]. Inglesfield found that the interference between the extrinsic and intrinsic plasmon is suppressed in the long wavelength plasmon excitations. The theoretical calculations by different groups predict an asymmetric line-shape for both bulk and surface plasmon[20,21,23,24].

Angle-dependent Al 2s XPS spectra for Al(111), recorded at nearly normal (80°) and grazing (10°) emission are shown in Figure 1. The monopole surface plasmon ($1w_s$) is observed at 128.4 eV binding energy (BE) or 10.4 eV loss energy. The main difference between normal and grazing emission is the large enhancement in the intensity of the monopole surface plasmon in grazing emission. The increase in intensity is about a factor of five. Besides the intensity increase, there is a drastic change in the $1w_s$ line-shape (thick solid lines in Figure 1). In normal emission, the surface plasmon has an unusual shape with a gradually decreasing intensity towards higher loss energy side and a step-like shape on the lower loss energy side (marked by arrow in Figure 1). The corresponding left and right Lorentzian widths, Γ_L and Γ_R, obtained from the least-square fitting, are 3.6 and 0.08 eV, respectively. In contrast, in grazing emission the surface plasmon is relatively more symmetric, although Γ_L (= 1.92 eV) is still larger than Γ_R (= 0.84 eV). Unlike the surface plasmon, the bulk plasmon ($1w_p$) intensity decreases in grazing emission by a factor of 2.4 compared to that in the normal emission. Although not as pronounced as the surface plasmon, the bulk plasmon line-shape is also somewhat asymmetric in normal emission and becomes more symmetric in grazing emission. The surface plasmon has more intensity compared to the bulk plasmon in the grazing emission, which was not observed in previous studies[7,8]. This is because the surface

plasmon intensity is highly sensitive to surface contamination. We have ensured that Al(111) surface is completely clean in the present work, and this was not so in the previous studies where residual oxygen contamination was reported[7,8]. The experimental technique and data analysis procedure have been described in ref. 45.

Since it is not possible to make a quantitative estimate of extrinsic, intrinsic and interference plasmons based only on experimental results, we have calculated the surface plasmon line-shape following the perturbation based method suggested by Inglesfield[21,22]. The details of the calculations are given in ref. 45. In agreement with the experiment, the calculated surface plasmon line-shape (J_{tot}) integrated over z is highly asymmetric and the step-like line-shape is well reproduced by the theory (Figure 2*a*). Discrepancy is however observed on the higher loss energy side: the experimental spectrum has larger intensity compared to that given by theory. We find that the $1w_s$ line-shape due to photoemission from only the surface ($z = 0$) has larger intensity on the higher loss side than the integrated line-shape, J_{tot}. Thus, a possible reason for the disagreement could be that the contribution of surface ($z = 0$) photoemission to the surface plasmon intensity is underestimated by the theoretical curve, J_{tot}. This is probably related to the choice of the weighting factor, which is based on a semi-classical approach assuming that the bulk extrinsic terms dominate[21,45].

The calculated intrinsic surface plasmon (J_{int}) line shape is asymmetric with a sharp peak at 9.45 eV loss energy with 0.1 eV FWHM (Figure 2*b*). The surprising observation is that the area under J_{ext} (centred around 9.6 eV loss energy with 0.7 eV FWHM) is more than J_{tot}. This is because the interference contribution (J_{intf}) is negative over the whole energy range. It has an asymmetric inverted peak at 9.45 eV loss energy with 0.15 eV FWHM. The negative value of the interference term signifies that the plasmon created by the outgoing photoelectron (extrinsic process) is absorbed by the localized photo-hole potential (intrinsic process) reducing the total intensity of the surface plasmon. In fact, at the minimum loss energy end of the plasmon feature (9.4 eV), the calculated plasmon intensity becomes zero due to the negative interference term. Thus, Figure 2*b* shows the importance of the interference term in determining the plasmon line shape. We find the ratio of the intrinsic, extrinsic and interference plasmon contributions to be 1 : 0.7 : –1.3 in normal emission and 1 : 3.6 : –1.3 in grazing emission for Al 2s related surface plasmon[45].

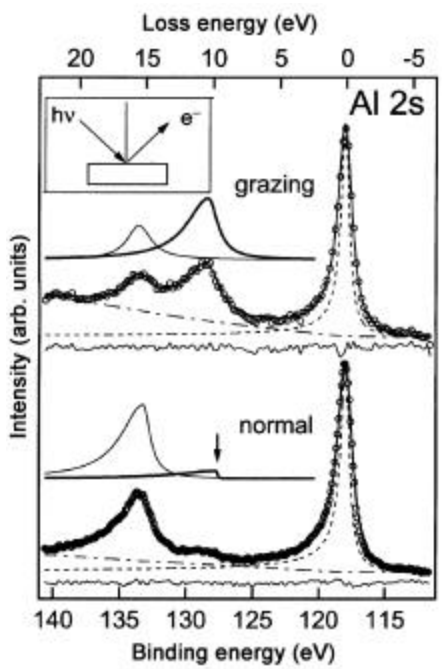

Figure 1. Plasmon features associated with the Al 2s spectra of Al(111) are shown. The monopole surface ($1w_s$) and bulk ($1w_p$) plasmon line shapes are compared between nearly grazing (10°) and normal (80°) emission. The no loss main peaks in both the spectra are normalized to the same intensity. Solid line through the experimental data (open circles) is the fitted curve. The residual for the fit, which is within the statistical scatter of the experimental data, is shown below each spectrum. The deconvoluted Al 2s Doniach–Sunjic line-shape (dashed line) and the inelastic background (dot-dashed line) are also shown. The surface (thick solid line) and bulk (thin solid line) plasmon line-shapes are shifted upwards for clarity of presentation. The step-like surface plasmon line-shape is indicated by an arrow. Inset shows the geometry of the experiment.

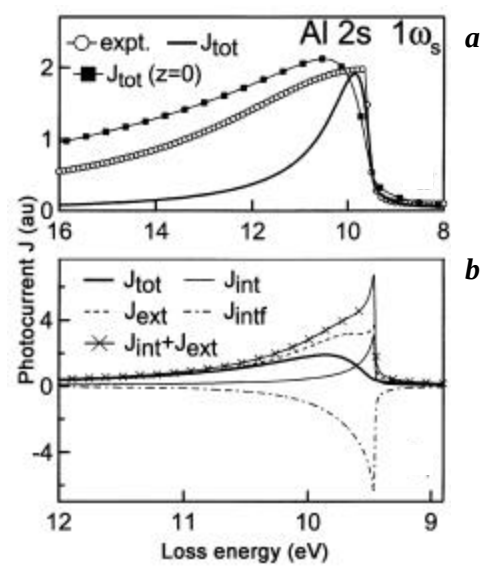

Figure 2. ***a***, Calculated monopole surface plasmon J_{tot} (thick solid line) is compared with the experimental Al 2s surface plasmon (open circles) recorded in normal emission (from Figure 1). The zero of the loss energy scale (not shown in the figure) refers to the no-loss peak position. J_{tot} ($z = 0$) (filled squares) is the surface plasmon corresponding to $z = 0$. ***b***, Calculated total (J_{tot}, thick solid line), intrinsic (J_{int}, thin solid line), extrinsic (J_{ext}, dashed line), interference (J_{intf}, dot-dashed line) and sum of extrinsic and intrinsic ($J_{int} + J_{ext}$, crosses) contributions to the Al 2s surface plasmon line-shape are shown in an expanded scale.

The multipole surface plasmon is expected to occur around 13 eV loss energy, but it is not clearly observed in the XPS spectra probably because it is dominated by the monopole surface plasmon. Another reason for absence of a separate multipole plasmon feature in the Al 2s and 2p XPS spectra is that, unlike in electron energy loss spectroscopy (EELS), contributions from all $k_{||}$'s are observed in photoemission. This probably results in a broad featureless line-shape for the multipole plasmon. Higher intensity in the experimental surface plasmon line shape around 13 eV (Figure 2 *a*) is probably related to the multipole plasmon, which is not considered in the above calculation. Using angle and energy resolved photoyield (AERPY) method, where only the $q = 0$ mode is observed, a huge enhancement occurs in the photoemission cross-section when the incident photon frequency is equal to the multipole plasmon frequency[26,46]. A representative AERPY spectrum for Al(111), taken in the constant initial state mode at 0.1 eV BE, is shown in Figure 3. The spectrum basically represents the normalized intensity of the Fermi edge of an ARPES spectrum in normal emission, as a function of incident photon energy[46]. The work function cut-off for the threshold of photoemission is observed at 4.5 eV. The peak at 13 eV is related to the decay of the multipole plasmon via electron-hole excitations, which enhances the photoemission signal. The multipole peak has a triangular shape (FWHM 3 eV) with a sharp increase in intensity below w_p. The width of the multipole plasmon in Al is in agreement with the total photoabsorption calculations[47]. We find the multipole plasmon frequency (w_m) relative to the bulk plasmon frequency to be $0.85w_p$. This is in good agreement with the time-dependent local density approximation (TDLDA) jellium calculation, which predicts[25] w_m to be $0.8w_p$. The dip indicated by w_p in Figure 3 corresponds to the bulk plasmon frequency. Feature B is related to bulk plasmon excitation with $q > 0$, while feature A varies with incidence angle and is explainable by Fresnel theory[46].

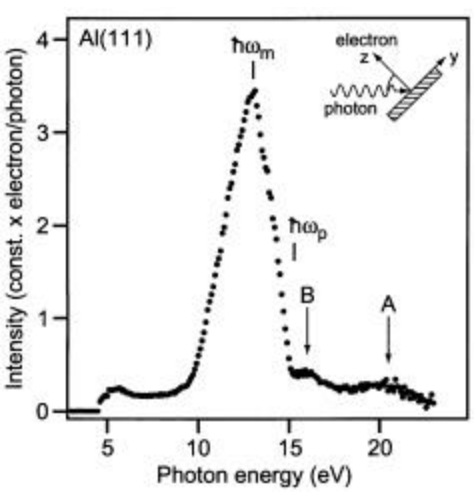

Figure 3. Angle and energy resolved photoyield (AERPY) spectrum of Al(111) showing the multipole plasmon (w_m). The geometry of the experiment is shown in the inset, the photon incidence angle is 45°.

Quantum well resonances in sodium thin films

Quantum well states are formed by the confinement of electronic states by the bounding potential barriers. For thin films, the confinement is in the direction perpendicular to the film by the ground state vacuum potential barrier on one side and the gap in the substrate band structure on the other[36]. Quantum well states in Na thin films on Cu(111) were explained by the electron confinement provided by the Cu sp band gap at the *L* point[48]. In case of Na/Al(111), this mechanism is absent since the band gap at *L* point does not exist. In this section, we discuss the origin of the observed quantum well resonances in Na thin films on Al(111). We find that the incident photons, which cause photoemission, themselves interact with the electron charge density in the overlayer[49].

ARPES spectra of Na adlayers of different thicknesses on Al(111) recorded in normal emission using synchrotron radiation are shown in Figure 4. The experimental details are given in ref. 49. The Al(111) spectrum (bottom), which is only about 1 eV wide for the photon energy of 5.5 eV, does not show any sharp features. Upon deposition of Na, the work function decreases and thus photoemission spectra over a larger BE range could be recorded. Feature A appears at a thickness of 1.5 monolayer (ML) near E_F. At 4.5 ML thickness, two more features appear at 0.8 (B) and 1.8 eV (F). Feature B shifts to 0.4 eV, while feature A is absent for 7.5 ML. For higher coverages, e.g. 15 ML, a new feature (C) appears at 0.5 eV. At subsequent

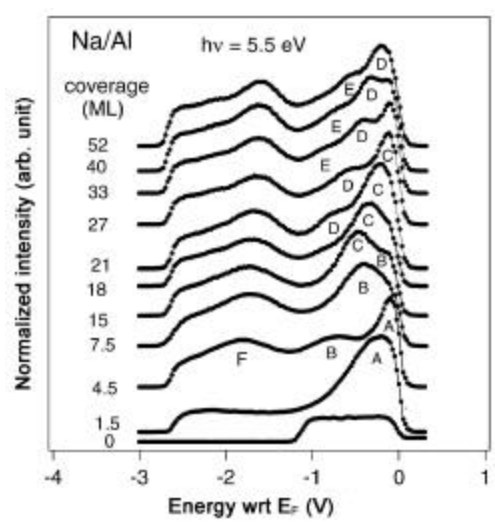

Figure 4. Angle resolved photoemission (ARPES) spectra recorded in normal emission with 5.5 eV photon energy for different Na coverages on Al(111). The features marked A–E are related to the quantum well resonances, while feature F is related to a direct transition.

coverages, feature C goes to lower BE until it reaches E_F at 33 ML coverage. Similar behaviour is observed for features D and E. So, we find that with increasing thickness of the overlayer, features appearing within 1 eV BE disperse towards E_F and actually seem to move across E_F. This behaviour is the well-known signature of quantum well states with $k_{||}$ quantization[36]. The observed features do not disperse with photon energy which rules out the possibility that these are due to direct transition[49]. The dispersion of these features with coverage also shows that these features are not surface states. From ARPES spectra (not shown in Figure 4, see ref. 49) recorded as a function of photon energy (4.5 to 8 eV), an enormous enhancement of the spectra is observed below 7 eV, with the maximum at 5.75 eV, which corresponds to the standing wave-like bulk plasmon mode of the Na film[50]. This behaviour differs fundamentally from ordinary quantum well states. It should be noted that feature F in Figure 4 remains largely stationary throughout the studied coverage range. The origin of this feature is related to a direct transition from the occupied Na s-band to an unoccupied band corresponding to epitaxial f.c.c. Na layer in (111) orientation. This is supported by the f.c.c. hexagonal (1×1) low energy electron diffraction (LEED) pattern observed for the Na layer. Thus, Na exhibits a pseudomorphic f.c.c. growth on Al(111).

Discretization of the Na band is possible even in absence of a reflecting band gap barrier in Al because of the negative potential step at the Na/Al interface. This negative potential step arises because of the difference in Fermi energy of Na and Al (see Figure 3 of ref. 49). Under normal circumstances these resonances are suppressed by the large signal from the substrate. The screening response of Na valence electrons to the incident photons generates an induced field normal to the surface, which together with the bare photon field forms the effective local field that governs the photoemission cross-section. In this case, due to screening, when the photon energy coincides with the bulk plasmon frequency of Na, the local electric field in the overlayer is about two orders of magnitude larger than the substrate. This has been calculated using time-dependent local density approximation[49]. Thus, the quantum well resonances due to the negative step potential are enhanced by tuning the photon energy to the collective overlayer modes, while emission from substrate bands is suppressed. Similar effect has been observed[51] in other systems like K/Al(111).

Argon nano-bubbles in Al(111)

Many interesting physical phenomena are observed in rare gas bubbles formed in Al. During ion bombardment many different processes take place, for example, sputtering of target atoms, scattering of incident ions, implantation in the target, sputtering of already implanted ions, formation of vacancies, di-vacancies, coalescence of vacancies with implanted atoms, formation of adatoms at the surface and formation of bubbles. In Al, after the ion bombardment, formation of bubbles is favoured compared to other defects. This has been established by theoretical calculations and different experimental techniques like EELS, X-ray absorption, TEM and STM[37–44]. Roussow *et al.*[39] studied Ar bubbles in Al with TEM using 50 keV ions implanted in an Al film of thickness 50 nm. They reported a bubble radius of 13.5 ± 2.5 Å. vom Felde *et al.*[38] investigated Ar, Ne and Xe bubbles in Al using EELS and they observed plasmons related to the bubble surface. The implanted Ar atoms form bubbles because of repulsive pseudopotential and negative heat of solution of the gas atoms in Al[37]. Schmid *et al.*[43] found a correlation between number of bubbles and the amount of implanted Ar. XPS and related theoretical calculations have been performed to understand why the core level BE of isolated implanted rare gas atoms in metals decrease with respect to their gas phase BE[52–54]. The decrease in BE was explained by screening of the core-hole by metal conduction electrons.

Figure 5 shows the Ar 2p core level spectra for 1 ML fluence for argon implanted in Al (Ar↓Al). 1 ML fluence or dose of Ar^+ ions is equivalent to the number of atoms on the Al(111) surface (1.415×10^{15} atoms/cm^2). Fluence was determined by measuring the bombardment-induced current through the sample and the geometry of the experiment. Details of the experimental and data analysis procedures are given in ref. 55. For 0.3 keV implantation energy (E_i), the BE of the Ar $2p_{3/2}$ peak is 242.3 ± 0.05 eV with respect to E_F, with a spin-orbit splitting of 2.1 ± 0.1 eV. The shift of the Ar 2p main peak between 0.3 and 3 keV implantation energy is found to be about 0.6 eV. A similar shift of 0.5 eV is also observed for Ar 2s.

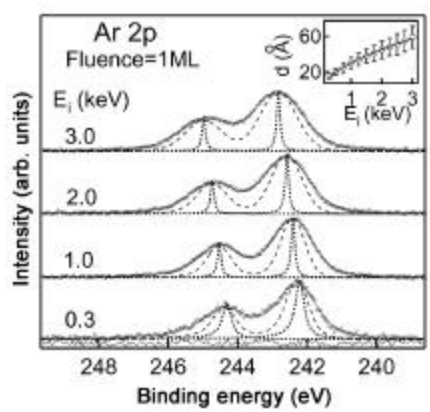

Figure 5. Ar 2p core level spectra (open circles), which have been background-subtracted and normalized to same intensity along with the fitted curve (thin solid line), as a function of E_i for 1 ML fluence. The deconvoluted DS line-shape (short dashes) and the spectral line shape including the Gaussian broadening but excluding the instrumental broadening (long dashes) are shown below each spectrum. The residual for the fit (for 0.3 keV spectrum) is within the experimental scatter. Inset shows the calculated projected range (d) as a function of E_i (open circles) and fitted curve (solid line); bars show the straggle.

In contrast, the corresponding Al 2p spectra do not exhibit any shift or change in line shape. We have recorded the spectra for many different E_i (0.3 to 3 keV) and fluence (0.025 to 3 ML) combinations. The core level shift is represented by ΔE_B, which is the decrease in Ar $2p_{3/2}$ BE in Ar↓Al from that of the gas phase (248.45 eV). In order to avoid confusion, we have referred both the BE's to the vacuum level of Al(111), which has a work function of 4.2 eV. The values of ΔE_B as functions of E_i and fluence are plotted in Figure 6 for different (E_i, fluence) combinations. For each combination, we have implanted Ar on clean Al, and not on an already implanted Al surface. We find that ΔE_B is relatively large (2.2–2.3 eV, blue region in Figure 6) for small values of E_i and fluence. On the other hand, for large E_i and fluence, ΔE_B is small (1.4–1.5 eV, red region). The difference between maximum and minimum values of ΔE_B turns out to be about 0.9 eV.

The decrease in BE with respect to gas phase, i.e. ΔE_B was related to the relaxation energy in previous studies on implanted rare gas atoms in metals[52–54]. The relaxation energy (ΔE_R) is the energy gained by the system through extra atomic screening by host metal conduction electrons in the final state of photoemission. ΔE_R was shown to be inversely proportional to the effective radius (R_a) of the rare gas atom using a linear response relaxation model[52]. Watson *et al.*[53] have reported ΔE_R for Ne, Ar, Kr and Xe to be 4.8, 4.0, 3.8, and 3.5 eV respectively. These values are found to vary linearly with $1/R_a$. Based on image potential model of classical electrostatics for a cavity in the metal host, the relaxation energy[54] is $e^2/2R_a$. Based on the above arguments we can write for Ar bubbles in Al

$$\Delta E_B = c_1/R + c_2, \tag{1}$$

where R is the average effective radius of the bubble and c_1 is the proportionality constant. c_2 represents contributions to ΔE_B which are independent of R. For example, ΔE_B will depend on the physical state of Ar since solid Ar has lower BE than gaseous Ar, and this would be independent of R. Similarly, the intra-atomic relaxation and the electrostatic shift due to the dipole barriers at Al surface and at bubble-Al interface would be independent of R.

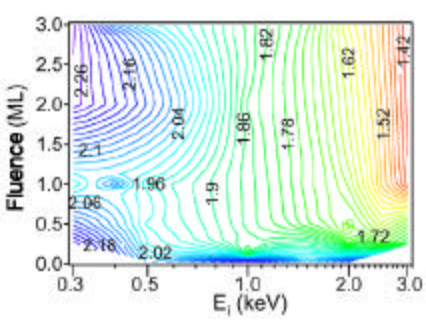

Figure 6. Contour plot showing the variation of ΔE_B as functions of E_i and fluence. In the rainbow colour scale, the violet contour corresponds to 2.3 eV, while the red contour corresponds to 1.4 eV.

Since change in R with implantation conditions has been reported earlier, Ar 2p BE variation could be explained by final state screening. With the motivation to examine whether R could depend on E_i, we note that if the projected range (d, i.e. the average depth of Ar atoms in Al) increases, a greater number of diffusion steps would be required for an Ar atom to reach the surface and desorb[56]. Hence, for larger d, the probability that Ar atoms would absorb vacancies or coalesce would increase, resulting in larger R. To find d as a function of E_i, we have performed Monte Carlo simulations using TRIM code[57]. 50,000 ions were used for each calculation. The Ar ions have been implanted in normal incidence geometry. In order to mimic the experimental conditions, the calculations were also performed in the normal incidence geometry on the Al substrate for different E_i values. We find that d increases from 16 to 60 Å as E_i is varied from 0.3 to 3 keV (inset, Figure 5). We find that an empirical relation $d \propto E_i^{0.6}$ describes the variation well and is in fair agreement with the previous theoretically derived result[58]. The above discussion provides an explanation as to why R should increase with E_i. It should be noted that voids formed during bombardment can act as trapping centres for Ar atoms and nucleate the formation of bubbles through absorption and coalescence. It has been recently reported that Ar ions incident on Al give rise to a thermal spike, which causes local melting and forms voids in the sub-surface[59]. These voids can act as nucleating centres for Ar bubbles. The void volume is reported to be proportional[59] to E_{nuc}, which is the energy available for nuclear collisions. From our TRIM calculations, we find that E_{nuc} is about 92% of E_i in this ion energy range. So, the void volume is approximately proportional to E_i, i.e. R is proportional to $E_i^{1/3}$. So, it can be argued that R would increase with E_i, based on which we propose a relation between R and E_i: $R = c_3 E_i^n$, where c_3 is a proportionality constant and n is an exponent. Substituting this in eq. (1), we get

$$\Delta E_B = c_1'/E_i^n + c_2. \tag{2}$$

We find that the variation of ΔE_B as a function of E_i is similar for different fluences above 0.025 ML and we fit these data with eq. (2) (Figure 7). We have freely varied all the different parameters like n, c_1' (= c_1/c_3), and c_2. The data is weighted by $1/s$, where σ is the standard deviation. We obtain $n = 0.5 \pm 0.2$, $c_1' = 0.4 \pm 0.2 \times 10^{-3}\ \mathrm{keV}^{(n+1)}$ and $c_2 = 1.4 \pm 0.2$ eV. The value of reduced c^2 is close to one (1.19), which indicates a reasonably good fit. The prediction bands show the region where the experimental data, considering random errors, would fall with 90% probability. No systematic deviation of the data from the fitted curve based on eq. (2) is observed from the residuals. These indicate the validity of eq. (2) in modelling the experimental data, implying that the variation of Al conduction electron screening strength related to change in R explains the observed Ar 2p BE shift. Although it is not possible

to determine c_3 separately from the above fitting, relative variation of R with E_i can be obtained. If we assume R to be R_o for $E_i = 0.3$ keV, we find R to increase from $1.3 \pm 0.15\,R_o$ (for 0.5 keV) to $3.2 \pm 1.8\,R_o$ (for 3 keV). We find that for very small fluence (0.025 ML) the Ar atoms are mostly isolated. If we take the radius of the isolated Ar atoms to be their van der Waals radius[60] (1.88 Å), then the radius of the bubbles can be determined relative to the radius of isolated Ar atoms. Thus, we find R to be 2.4 ± 0.3 Å, 3.4 ± 0.9 Å, and 6 ± 3.4 Å for 0.5, 1 and 3 keV, respectively. Although this method of determining R is somewhat indirect, the trend is in agreement with TEM results[39,40] and this further supports our explanation for the BE variation[55].

Ar bubbles in Al are reported to be in the solid phase at room temperature and are pressurized to about 25 to 60 kbar[40,41]. So, an alternative explanation for the above BE shift could be the compression of the core electron wave functions due to the variation of pressure with R, particularly since R is reported to be inversely proportional to pressure[40]. In order to calculate the influence of pressure on ΔE_B, we have performed relativistic *ab-initio* full potential linear augmented plane wave (FPLAPW) calculations using the WIEN97 code[61]. Since the lattice constant of solid Ar (a = 5.26 Å at 4.2 K and standard pressure) has been experimentally determined as a function of pressure[62], we have performed the calculations[63] by contracting the f.c.c. lattice of Ar (since Ar is in solid state in the bubble) at steps of 2% to a maximum of 12% (a = 4.629 Å)[62]. We find a small variation of 0.1 eV in Ar $2p_{3/2}$ BE between standard and 60 kbar pressure, as compared to the large experimentally observed BE shift of 0.9 eV. This is expected because the core-level wave functions (2p) are highly localized compared to the outer levels (3s, 3p). Hence, the possible explanation of change in pressure causing the BE shift is ruled out.

In the photoemission process, the electrons are ejected from the solid leaving a core-hole behind. This is the final state of photoemission whose life-time is about 10^{-16} s. Screening response of conduction electrons to the core-hole in the final state of photoemission occurs within this time scale. In case of metals, a well-known manifestation of this screening response is the Doniach–Sunjic asymmetry of the core level line-shape[64]. This results from infinitesimal electron-hole excitations across E_F due to the screening response of the conduction electrons to the sudden creation of the core-hole. Thus, the out-going photoelectron loses energy and this causes an asymmetric line shape on the higher BE side of the core level peak. The extent of this asymmetry is quantified by the Doniach–Sunjic asymmetry parameter, a. Langreth found a to be related to the core-hole potential (V_Q) by the following expression[65]

$$a = \sum_{q<2q_F} |V_Q|^2 / |e(q,\ 0)|^2 \times N(0)/qV_F, \qquad (3)$$

where $N(0)$ is the density of states at E_F and e is the dielectric function. The band gap of solid Ar varies from 8.9 to 9.6 eV between normal and 60 kbar pressure[55]. Hence, for solid Ar, a should be zero because of the bandgap. In contrast, for Ar in Al, we find a to be sizeable (0.06 ± 0.07), as compared to, for example, $a = 0.11$ for Al. We find a to vary between 0.01 and 0.06, depending on E_i and fluence. This is shown as a contour plot in Figure 8. a is non-zero in Ar↓Al because of the screening by Al conduction electrons in response to the Ar core-hole potential, V_Q. Interestingly, comparing Figures 6 and 8, we find that there is an overall similarity in the variation of a and ΔE_B with E_i and fluence. This demonstrates that both these effects are related to the same physical phenomenon, namely screening by electrons. In fact, it has been theoretically shown that BE shift due to screening depends on the square of hole charge density[52], which is related to V_Q^2 on which a depends according to eq. (3). An asymmetry observed in Ne 1s for Ne implanted in Cu has been related to screening induced BE shift due to formation of Ne clusters and the authors state[54] that the number of these Ne clusters would increase with E_i. For Ar↓Al, this explanation is not valid because in that case asymmetry would increase with E_i and fluence. Instead, we find that for large E_i and fluence, a is small (0.01)

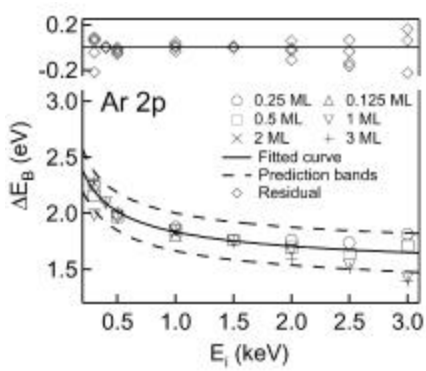

Figure 7. ΔE_B as a function of E_i for different fluences with fitted curve (solid line) and 90% prediction bands (dashed lines). Residuals are shown at the top of the graph.

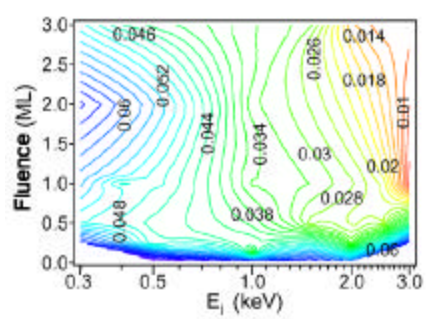

Figure 8. Contour plot showing the variation of the Doniach–Sunjic asymmetry parameter (a) as functions of E_i and fluence. In the rainbow colour scheme, the violet contour corresponds to $a = 0.074$, and the red contour to $a = 0$.

(Figure 8); while for small E_i and fluence, i.e. small R, a is large (0.06). This is because for small R, the Al conduction electron screening cloud is more compact and as R increases a decreases because of reduced screening.

1. Lundqvist, B. I., *Phys. Kondens. Mater.*, 1969, **9**, 236.
2. Langreth, D. C., *Phys. Rev. Lett.*, 1971, **26**, 1229.
3. Pardee, W. J. *et al.*, *Phys. Rev. B*, 1975, **11**, 3614.
4. Fuggle, J. C., Fabian, D. J. and Watson, L. M., *J. Electron Spectrosc. Rel. Phenom.*, 1976, **9**, 99.
5. van Attekum, P. M. Th. and Trooster, J. M., *Phys. Rev. B*, 1978, **18**, 3872; 1979, **20**, 2335.
6. Steiner, P., Hoechst, H. and Huefner, S., *Z. Physik B*, 1978, **30**, 129; Hoechst, H., Steiner, P. and Huefner, S., *Z. Physik B*, 1978, **30**, 145.
7. Bradshaw, A. M., Domcke, W. and Cederbaum, L. S., *Phys. Rev. B*, 1977, **16**, 1480.
8. Baird, R. J. *et al.*, *Surf. Sci.*, 1978, **72**, 495.
9. Smith, N. V. and Spicer, W. E., *Phys. Rev. Lett.*, 1969, **23**, 769.
10. Baer, Y. and Busch, G., *Phys. Rev. Lett.*, 1973, **30**, 280; Citrin, P. H., Wertheim, G. K. and Baer, Y., *Phys. Rev. B*, 1977, **16**, 4256.
11. Kowalczky, S. P. *et al.*, *Phys. Rev. B*, 1973, **8**, 3583; Pollak, R. A. *et al.*, *J. Electron Spectrosc.*, 1974, **3**, 381.
12. Flodstrom, S. A. *et al.*, *J. Vac. Soc. Technol.*, 1977, **14**, 303.
13. Norman, D. and Woodruff, D. P., *Surf. Sci.*, 1979, **79**, 76.
14. Chang, J. J. and Langreth, D. C., *Phys. Rev. B*, 1972, **5**, 3512; 1973, **8**, 4638.
15. Mahan, G. D., *Phys. Stat. Solidi B*, 1973, **55**, 703.
16. Feibelman, P. J., *Phys. Rev. B*, 1973, **7**, 2305.
17. Langreth, D. C., In *Collective Properties of Physical Systems* (eds Lundquist, B. and Lundquist, S.), Academic, New York, 1974.
18. Sunjic, M., Sokcevic, D. and Lucas, A., *J. Electron Spectrosc.*, 1974, **5**, 963.
19. Sunjic, M. and Sokcevic, D., *Solid State Commun.*, 1974, **15**, 165; Sokcevic, D. and Sunjic, M., *Solid State Commun.*, 1974, **15**, 1703.
20. Penn, D. R., *Phys. Rev. Lett.*, 1977, **38**, 1429; *ibid*, 1978, **40**, 568.
21. Inglesfield, J. E., *Solid State Commun.*, 1981, **40**, 467.
22. Inglesfield, J. E., *J. Phys. C: Solid State Phys.*, 1983, **16**, 403.
23. Bose, S. M., Prutzer, S. and Longe, P., *Phys. Rev. B*, 1983, **27**, 5992.
24. Hedin, L. H., In *X-ray Spectroscopy* (ed. Azaroff, L. V.), McGraw-Hill, New York, 1974, p. 226.
25. Liebsch, A., *Elementary Excitation on Metal Surfaces*, Plenum, New York, 1997.
26. Plummer, E. W., *Solid State Commun.*, 1992, **84**, 143.
27. Miller, T., McMohan, W. C. and Chiang, T.-C., *Phys. Rev. Lett.*, 1996, **77**, 1167.
28. Hansen, E. D., Miller, T. and Chiang, T.-C., *Phys. Rev. Lett.*, 1997, **78**, 2807.
29. Claessen, D. *et al.*, *Phys. Rev. Lett.*, 1999, **82**, 1740.
30. Bennett, A., *Phys. Rev. B*, 1970, **1**, 203.
31. Eguiluz, A., Ying, S. C. and Quinn, J. J., *Phys. Rev. B*, 1975, **11**, 2118.
32. Inglesfeld, J. E. and Wikborg, E., *J. Phys. F*, 1975, **5**, 1706.
33. Schwartz, C. and Schaich, W. L., *Phys. Rev. B*, 1984, **30**, 1059.
34. Kempa, K. and Gerhardts, R. R., *Solid State Commun.*, 1985, **53**, 579.
35. Tsuei, K.-D. *et al.*, *Surf. Sci.*, 1991, **247**, 302.
36. Wachs, A. L. *et al.*, *Phys. Rev. B*, 1986, **33**, 1460; Miller, T. *et al.*, *Phys. Rev. Lett.*, 1988, **61**, 1404; Ortega, J. E. *et al.*, *Phys. Rev. B*, 1993, **47**, 1540.
37. Inglesfield, J. E. and Pendry, J. B., *Philos. Mag.*, 1976, **34**, 205.
38. vom Felde, A. *et al.*, *Phys. Rev. Lett.*, 1984, **53**, 922.
39. Rossouw, C. J. and Donnelly, S. E., *Phys. Rev. Lett.*, 1985, **55**, 2960.
40. Fink, J., *Adv. Electron. Electron Phys.*, 1989, **75**, 121.
41. Faraci, G. *et al.*, *Phys. Rev. B*, 1991, **43**, 9962.
42. Rife, J. C. *et al.*, *Phys. Rev. Lett.*, 1981, **46**, 1220.
43. Schmid, M. *et al.*, *Phys. Rev. Lett.*, 1996, **76**, 2298.
44. Arzt, E., *J. Appl. Phys.*, 1994, **76**, 1563.
45. Biswas, C. *et al.*, *Phys. Rev. B*, 2003, **67**, 165416.
46. Barman, S. R., Haeberle, P. and Horn, K., *Phys. Rev. B*, 1998, **58**, R4285.
47. Feibelman, P. J., *Prog. Surf. Sci.*, 1982, **12**, 287; Liebsch, A. *et al.*, *Surf. Sci.*, 1994, **302**, 303.
48. Lindgren, S. A. and Wallden, L., *Phys. Rev. Lett.*, 1987, **59**, 3003; *Phys. Rev. B.*, 1988, **38**, 3060.
49. Barman, S. R. *et al.*, *Phys. Rev. Lett.*, 2001, **86**, 5108.
50. Barman, S. R. *et al.*, *Phys. Rev. B*, 1998, **57**, 6662.
51. Barman, S. R. *et al.* (unpublished).
52. Waclawski, B. J. *et al.*, *Phys. Rev. Lett.*, 1978, **41**, 583.
53. Watson, R. E. *et al.*, *Phys. Rev. B*, 1976, **14**, 18.
54. Citrin, P. H. and Hamann, D. R., *Phys. Rev. B*, 1974, **10**, 4948.
55. Biswas, C. *et al.*, *Phys. Rev. Lett.*, 2004, **92**, 115506.
56. Reed, D. J., *Rad. Effects*, 1977, **31**, 129.
57. Biersack, J. P. and Haggmark, L., *Nucl. Instrum. Meth.*, 1980, **174**, 257 (TRIM code is available free of cost from www.srim.org)
58. Martan, J., *Nucl. Instrum. Meth. Phys. Res. B*, 1984, **2**, 202.
59. Busse, C. *et al.*, *Phys. Rev. Lett.*, 2000, **85**, 326.
60. Bondi, A., *J. Phys. Chem.*, 1964, **68**, 441.
61. Blaha, P. *et al.*, WIEN97 (Karlheinz Schwarz, Techn. Universitat Wien, Austria), 1999. ISBN 3-9501031-0-4.
62. Finger, L. W. *et al.*, *Appl. Phys. Lett.*, 1981, **39**, 892.
63. Chakrabarti, A. *et. al.* (to be published).
64. Doniach, S. and Sunjic, M., *J. Phys C*, 1970, **3**, 285.
65. Langreth, D. C., *Phys. Rev. B*, 1970, **1**, 471.

ACKNOWLEDGEMENTS. I gratefully acknowledge the contributions from Ms C. Biswas, Mr A. K. Shukla, Ms S. Banik, Dr Aparna Chakrabarti, Prof. K. Horn, Prof. A. Liebsch, Prof. P. Haeberle and Dr J. A. Maytorena who have been the collaborators in the work discussed in this review. Prof. Horn is specially thanked for his constant help and encouragement. Prof. V. N. Bhoraskar, Dr B. A. Dasannacharya and Prof. A. Gupta are thanked for support. I thank DST, New Delhi for financial support.